Delft University of Technology

Time-varying, ray tracing irradiance simulation approach for photovoltaic systems in complex scenarios with decoupled geometry, optical properties and illumination conditions

Calcabrini, Andres ; Cardose, Ruben; Gribnau, David; Babal, Pavel; Manganiello, Patrizio; Zeman, Miro; Isabella, Olindo

Important note
To cite this publication, please use the final published version (if applicable).
Please check the document version above.

RESEARCH ARTICLE

PROGRESS IN
PHOTOVOLTAICS WILEY

Time-varying, ray tracing irradiance simulation approach for photovoltaic systems in complex scenarios with decoupled geometry, optical properties and illumination conditions

Calcabrini Andres[1] ![ORCID] | Cardose Ruben[1] | Gribnau David[1] | Babal Pavel[2] |
Manganiello Patrizio[1] ![ORCID] | Zeman Miro[1] | Isabella Olindo[1]

[1]Department of Electrical Sustainable Energy, Delft University of Technology, Delft, The Netherlands

[2]Kipp & Zonen BV, Delft, The Netherlands

Correspondence
Manganiello, Patrizio, Department of Electrical Sustainable Energy, Delft University of Technology, Delft, The Netherlands.
Email: p.manganiello@tudelft.nl

Abstract

The accurate computation of the irradiance incident on the surface of photovoltaic modules is crucial for the simulation of the energy yield of a photovoltaic system. Depending on the geometrical complexity of the surroundings, different approaches are commonly employed to calculate the irradiance on the photovoltaic system. In this article, we introduce a backward ray tracing simulation approach to calculate the irradiance on photovoltaic systems in geometrically complex scenarios. We explain how the repetition of time-consuming simulation steps can be avoided with the proposed approach by storing a selection of the results from the most computationally expensive parts of the problem, and we show that the irradiance calculated with the proposed approach is in good agreement with the results of Radiance, a well-established irradiance simulation tool. Furthermore, we present an experimental validation carried out using a pyranometer and a reference cell over a period of 6 months in a complex scenario, which shows errors lower than 5% in the calculation of the daily irradiation. Finally, we compare high-resolution spectral simulations with measurements taken with a spectroradiometer under different sky conditions. The proposed approach is particularly well-suited for the simulation of bifacial and tandem photovoltaic modules in complex urban environments, for it enables the efficient simulation of high-resolution spectral irradiance in scenarios with time-varying reflectance properties.

KEYWORDS
bifacial PV, irradiance modelling, ray tracing, spectral irradiance, tandem PV, urban PV

1 | INTRODUCTION

The developments in the photovoltaic (PV) field over the last decades have fostered the deployment of PV modules from utility-scale power plants to buildings[1,2] to vehicles.[3,4] As a result, many PV systems are installed in landscapes with complex geometries where PV modules are often subject to partial shading. Moreover, partially shaded PV systems will become increasingly common since the integration of PV in the urban environment will be of utmost importance for the development of net-zero-energy districts and the achievement of the UN Sustainable Development Goals.[5] In these scenarios, sophisticated simulation models are required to calculate

the irradiance incident on the solar cells and, subsequently, the electrical yield of a PV system.

The selection of an adequate irradiance simulation model for a specific application depends mainly on the size of the PV system and the complexity of the landscape surrounding the installation. Since the accuracy of the models increases proportionally to the required computing power and computation time, there is not a single model that is adequate for every application. The most common irradiance simulation models for PV applications can be classified in three main groups: transposition models, view factor models and ray tracing models.

Transposition models determine the irradiance incident on a PV module by adding the contributions of the beam, diffuse and ground reflected sunlight components on the plane of array (PoA). The diffuse component can be determined using one of several sky diffuse models that make different levels of approximations to describe the radiance distribution over the sky dome.[6–8] Transpositions models are the simplest and fastest approach to calculate the PoA irradiance. For example, the irradiance impinging on each cell of a 72-cell PV module can be simulated with 1-min resolution for an entire year using the simplified Perez diffuse sky model[7] in a few seconds with a modern personal computer. The main limitation of transposition models is the low accuracy in the calculation of the diffuse and reflected irradiance components. In a simple landscape, the expected simulation error is typically below 10%.[9] However, errors can increase to about 15% when the PV module is not optimally oriented.[10,11] Further limitations of these models are the underlying assumptions that the ground is uniformly illuminated and its reflectivity is constant.[12] As a result, transposition models are mostly used to simulate the irradiance on monofacial PV modules in relatively open landscapes such as large PV power plants or on rooftop PV systems in areas with low building density.

View factor models calculate the ground reflected irradiance component by computing the view factors from the PV module to the shaded and unshaded areas on the ground. This refinement makes view factor models suitable for simulating the irradiance on the rear side of modules in bifacial PV power plants. In addition, view factor models can be classified in two main types. The first type, usually referred to as 2D view factor models, assumes that rows of modules are infinitely long to simplify the calculation of view factors.[13] Two-dimensional view factor models have been implemented in commercial software packages[14] and errors lower than 16% have been reported in the calculation of the rear side irradiance.[15] The second type of view factor models, usually referred to as 3D view factor models,[16–19] considers that rows of PV modules are finite in length, which allows to include edge effects in the simulations. Experimental studies have reported errors that range from 5% to 15% in the rear side irradiance calculation.[20,21] Three-dimensional view factor models are also quite fast because the view factors are computed with closed-form formulas.[22] However, these formulas are not directly applicable in geometrically complex scenarios with non-horizontal surfaces, such as urban environments. In these cases, the estimation of view factors can be achieved by means of ray casting methods.[23]

Ray tracing (RT) models are the most general irradiance simulation approach and enable the simulation of surfaces with arbitrary orientations and bidirectional scattering distribution functions (BSDF).[24] RT algorithms are classified in two main types, forward and backward RT. Forward RT (FRT) algorithms calculate the irradiance on the PV module by tracing rays from the light sources (i.e., the sun and the sky dome) to the PV module and its surroundings.[25] FRT is often ineffective because most of the traced rays do not contribute to the computation of the irradiance on the PV module. In comparison, backward RT (BRT) algorithms calculate the irradiance on the PV module by following the path of rays from the PV module to the light sources, which significantly reduces the number of rays needed to compute the incident irradiance. In practice, BRT is mainly employed to solve the irradiance incident on the front (or back) surface of a PV module and FRT is typically used in combination with wave optics to solve the reflection and absorption in the internal layers of the PV module and the solar cells.[26–28] Radiance[29] is the most widely adopted backward ray tracer in the field of photovoltaics.[30–34]

In order to alleviate the computational time, RT models are usually employed to calculate daylight coefficients,[35] which are defined as the ratio between the irradiance incident on a target surface to the radiance emitted by a specific sky sector. Daylight coefficients are calculated to decouple the illumination conditions from the ray tracing solution of a specific geometry.[36] RT models provide a practical method to calculate daylight coefficients and to generate sensitivity maps[25] or daylight coefficient matrices.[32] These maps or matrices can then be multiplied by the sky radiance to calculate the irradiance on the solar cells under different sky conditions without repeating the ray tracing simulations.

Two main desirable features for irradiance models, which are not readily available in current ray tracing models, are the ability to perform spectrally-resolved simulations and to simulate surfaces with time-varying optical properties. Spectrally resolved irradiance simulations are important for bifacial PV systems[37–39] and will be essential in the near future to simulate the yield of tandem PV modules.[40,41] Meanwhile, the ability to simulate time-varying optical properties can be useful to model the effects of rain and snow on the surface reflectivity[42] and improve the calculation of the bifacial energy gain in large PV power plants.[43] Whereas the implementation of these features in transposition and view factor models is rather simple, adding these simulation capabilities to existing RT implies a heavy computational burden. Considering that daylight coefficients depend on the wavelength-specific optical properties of the surfaces composing the scene, ray tracing simulations should be repeated to calculate daylight coefficients at every wavelength and for every possible combination of optical properties.

In this article, we propose a backward ray tracing model to compute the irradiance on PV modules in scenarios with arbitrarily oriented diffuse and specular surfaces. The main novelty in this approach, is that the ray tracing calculations, the illumination conditions and the optical properties of the materials are decoupled. As a consequence, it is possible to avoid the repetition of the highly time-consuming ray tracing calculations when considering surfaces with
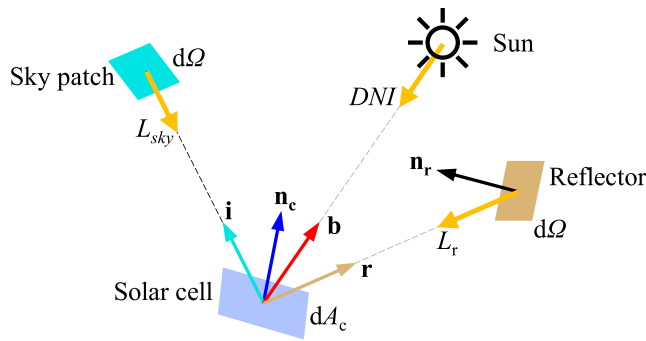
FIGURE 1 Irradiance components incident on a differential area of a solar cell dA_c. The beam component originates in the Sun, the diffuse component emanates from the sky dome and the reflected component comes from surfaces around the solar cell

time-varying optical properties and performing spectrally resolved irradiance simulations.

This article is organised in the following way. In Section 2, relevant radiometry concepts are presented. The proposed approach is described in detail in Section 3. In Section 4, the model is validated with measurements taken with different sensors at the PVMD monitoring station in Delft, the Netherlands. Finally, conclusions are presented in Section 5.

2 | BASIC RADIOMETRIC CONCEPTS

The irradiance G on a differential area element of a solar cell dA_c is defined as the total incident radiant flux $d\Phi$ per unit area. G can be divided into three components depicted in Figure 1: (1) The beam irradiance (G_{beam}) due to the radiant flux coming from the sun disk; (2) the diffuse irradiance (G_{diff}) due to the radiant flux coming directly from the sky dome; and (3) the reflected irradiance (G_{refl}) due to the radiant flux that bounces on the surface of objects in the scene before reaching the solar cell[*]:

$$G_{tot} = \frac{d\Phi}{dA_c} = G_{beam} + G_{diff} + G_{refl} \tag{1}$$

Assuming that the Sun is a point source, the beam irradiance can be calculated using Equation (2) from the direct normal irradiance (*DNI*), and the scalar product of the normal vector to the solar cell $\mathbf{n}_c$ and the vector that points from the centre of the solar cell to the centre of the solar disk $\mathbf{b}$:

$$G_{beam} = DNI \, (\mathbf{b} \cdot \mathbf{n}_c) \tag{2}$$

---
[*]All the vectors in the equations of this article are unitary vectors.

The diffuse irradiance can be determined by integrating the sky radiance L_{sky} incident from direction $\mathbf{r}$ over the visible part of the sky Ω_V:

$$G_{diff} = \int_{\Omega_V} L_{sky}(\mathbf{r}) \, (\mathbf{r} \cdot \mathbf{n}_c) \, d\Omega = \pi \int_{\Omega_V} L_{sky}(\mathbf{r}) \, dF_{c \to s} \tag{3}$$

where $d\Omega$ is the solid angle of a differential sky sector (i.e., sky patch). The second integral in Equation (3) is expressed in terms of the view factor from the differential area of the solar cell to a differential area element of the sky, which is defined as:

$$dF_{c \to s} = \frac{1}{\pi} \, (\mathbf{r} \cdot \mathbf{n}_c) \, d\Omega \tag{4}$$

Likewise, the reflected irradiance can be calculated by integrating the reflected radiance L_r incident from direction $\mathbf{r}$ over the part of the sphere around the solar cell that is blocked by surrounding reflective surfaces Ω_B:

$$G_{refl} = \int_{\Omega_B} L_r(\mathbf{r}) \, (\mathbf{r} \cdot \mathbf{n}_c) \, d\Omega \tag{5}$$

The reflected radiance L_r is determined by the radiance incident on the reflector and its optical properties described by the Bidirectional Reflectance Distribution Function (*BRDF*). The *BRDF* of an opaque reflective surface with normal $\mathbf{n}_r$, is defined as the ratio between the outgoing radiance dL_r in direction $\mathbf{r}$ to the radiance incident L_i from direction $\mathbf{r}$:

$$L_r(\mathbf{r}) = \int_{\Omega_H} dL_r(\mathbf{r}) = \int_{\Omega_H} BRDF(\mathbf{r}, \mathbf{r}) \, L_i(\mathbf{r}) \, (\mathbf{r} \cdot \mathbf{n}_r) \, d\Omega \tag{6}$$

where Ω_H is the hemisphere in front of the reflective surface.

It must be noted that the incident radiance on each reflector L_i depends on higher order reflections. Since the radiance incident on the reflector (L_i) must be the emitted or reflected radiance at a point on another surface, L_r is defined in terms of itself.[44] Therefore, practical methods, such as ray tracing, are needed to limit the recursivity of the problem and approximate the reflected irradiance on a solar cell.

3 | THE PROPOSED SIMULATION APPROACH

The irradiance simulation approach described in this section is based on a deterministic backward ray tracer limited to two ray bounces, which allows to simulate Lambertian and specular reflectors. The novelty of the approach lies in the order in which calculations are performed and the selection of results that are saved to reduce the computation time.
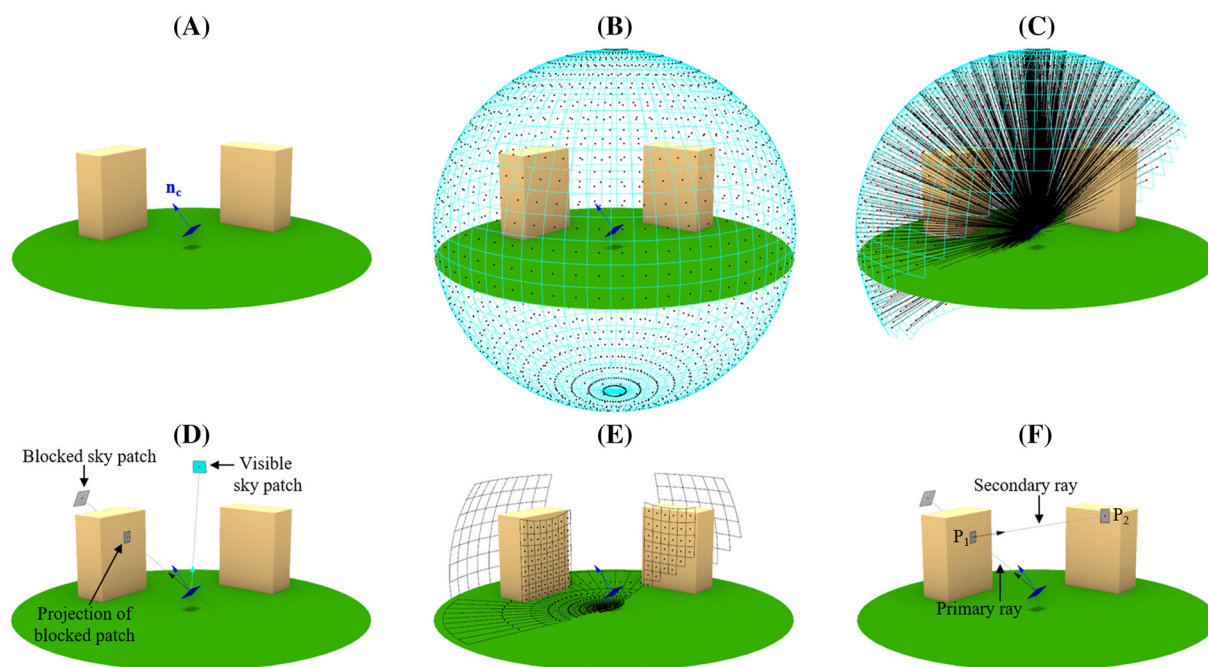
3.1 | Ray tracing

When surfaces in the scene have arbitrary shapes and orientations, it is not possible to calculate view factors using closed-form formulas as in 3D view factor models and the scene must be sampled by casting rays. In this section, the scene in Figure 2A is used to illustrate the steps of the ray tracing algorithm in the proposed approach.

First, a deterministic hemispherical sampling is performed by discretising an imaginary sphere centred at the solar cell as shown in Figure 2B. In Figure 2B, an equiangular discretisation is applied, yet it is important to note that the method is not limited to this specific discretisation. With the sky discretisation, the view factors from the solar cell to each sky patch ($dF_{c \to s}$) are determined by the position (**s**) and the solid angle of the sky patch ($d\Omega$) as expressed in Equation (4).

Next, primary rays are cast from the centre of the solar cell to the centroids of the sky patches in front of the cell (Figure 2C). Intersections between the scene and the rays can be solved combining an appropriate data structure (e.g., octrees and kD-trees) with efficient ray-surface intersection algorithms (e.g., Möller-Trumbore[45]). Rays that do not intersect with surfaces in the scene correspond to sky patches that are visible from the solar cell ("visible sky patch" in Figure 2D). For rays that intersect with surfaces in the scene, the projections of the corresponding sky patches at the intersection points are considered ("projection of blocked patch" in Figure 2D). It should be noted that the view factor from the solar cell to each blocked sky patch (in Figure 2E) is equal to the view factor from the solar cell to the corresponding projected patches. A list with all the blocked rays and the indices of the corresponding intersected surfaces is stored in memory after the primary ray tracing.

A second independent hemispherical sampling is performed with a higher angular resolution from the centre of the solar cell to generate a shadow map. A shadow map is a binary representation of the sky visibility from a given point in the scene, and it will be used to calculate the beam irradiance component. To generate shadow maps only rays that point forward from the solar cell and to the sky need to be traced. An example of a shadow map is shown in Figure 3, where
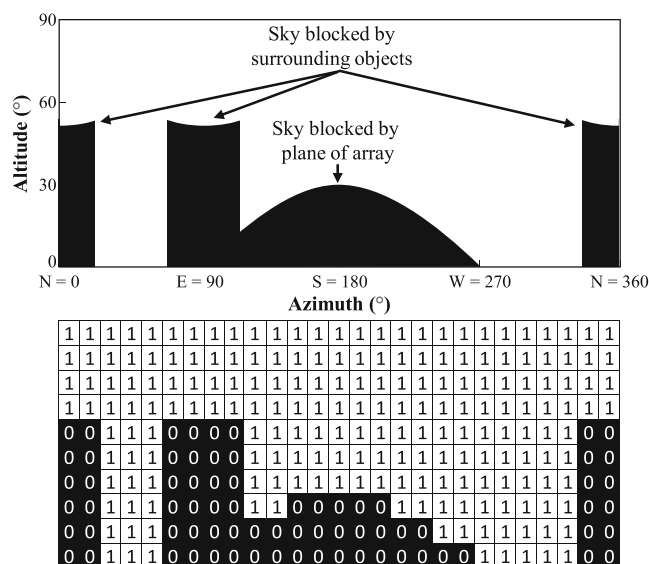
FIGURE 3 Shadow map. This shadow map corresponds to the solar cell in Figure 2A, which is facing North and tilted 30°. The angular resolution of this map was chosen for illustrative purposes. The typical resolution of a shadow maps is 1° or better

FIGURE 2 Graphical representation of the proposed ray tracing approach. (A) Example of a solar cell surrounded by two obstacles. (B) Spherical discretisation. (C) Hemispherical sampling. (D) Visible and blocked sky patches. (E) Projection of the blocked patches on the surfaces intersected by the primary rays. (F) Primary and secondary rays

the zeros correspond to sky patches blocked by the objects on the scene and ones to visible sky patches. The resulting shadow map is stored in memory. Shadow maps are binary arrays and require very limited storage space despite the high angular resolution. Approximately, 1000 shadow maps with an angular resolution of $1°$ occupy only 3 MB.

Then, for each intersection point between a primary ray and the scene (i.e., for every primary intersection point), the simulation develops differently depending on the type of intersected surface. If the intersected surface is an ideal specular reflector, a single secondary ray is cast from the primary intersection point. The direction of the secondary ray is given by the specular reflection of the primary ray on the intersected surface. If the secondary ray does not intersect with the scene, the index of the pointed sky patch is associated with the specular reflector patch and stored in memory, otherwise it is neglected. Otherwise, if the surface intersected by the primary ray is a Lambertian reflector, a secondary hemispherical sampling is performed from the primary intersection point (e.g., P_1 in Figure 2F). Again, some of the rays cast during the secondary hemispherical sampling will reach the sky and some will intersect with surfaces in the scene at secondary intersection points (e.g., P_2 in Figure 2F). The results of each of the secondary hemispherical samplings are stored in memory, same as in the case of the primary sampling. A shadow map is also generated and stored at every primary intersection point on a Lambertian reflector.

Finally, at each secondary intersection point (e.g., P_2 in Figure 2F), the proposed approach only calculates the beam and diffuse irradiance contributions. For this purpose, a tertiary hemispherical sampling is performed to generate shadow maps at every secondary intersection point. The shadow map, the secondary intersection point and the normal to the intersected surface are also stored in memory. To reduce the number of hemispherical samplings, new shadow maps are only calculated when a new intersection point is further than a specific user-defined distance from all previously calculated and stored intersection points.[†]

The described ray tracer only distinguishes between specular and diffuse reflectors. Therefore, the results of the hemispherical samplings and the shadow maps stored in memory are independent from the sky radiance and the reflectivity of the surfaces in the 3D model. Once the ray tracing calculations are completed, the irradiance is calculated as explained in the following section.

3.2 | Irradiance calculation

The beam irradiance incident on the solar cell is calculated by multiplying Equation (2) by the shading factor (SF), a time-dependent binary function defined in Equation (7). The shading factor indicates when the sun is blocked by the surroundings and it can be easily determined using shadow maps as look-up tables.

[†]In this work this parameter was set to 0.2 m

$$SF(t) = \begin{cases} 1 & \text{if the sun is visible,} \\ 0 & \text{if the sun is blocked,} \end{cases} \tag{7}$$

The discrete form of Equation (3) is used to calculate the diffuse component of the irradiance incident on the solar cell using the view factors from the cell to the unobstructed sky patches. In this work, the diffuse sky radiance (L_{sky}) in Equation (3) is calculated using Perez sky radiance distribution model.[46]

The irradiance contribution of specular reflectors is calculated considering that the *BRDF* is a Dirac delta function. Then, the irradiance contribution of an ideal specular patch with normal $\mathbf{n_r}$ and solid angle $d\Omega_r$ intersected by a primary ray with direction $\mathbf{r_1}$ is given by

$$\begin{aligned} dG_{refl} &= L_{sky}(\mathbf{p}) F_R(\mathbf{p}, \mathbf{n_r})(\mathbf{r_1} \cdot \mathbf{n_c}) d\Omega_{r1} \\ &= \pi L_{sky}(\mathbf{p}) F_R(\mathbf{p}, \mathbf{n_r}) dF_{c \to r1} \end{aligned} \tag{8}$$

where $\mathbf{p}$ is the specular reflection of $\mathbf{r_1}$ about $\mathbf{n_r}$, and F_R is the Fresnel factor which also depends on the refractive indices of the specular material (n) and the air (n_{air}).

In the case of Lambertian reflectors with normal $\mathbf{n_r}$ and solid angle $d\Omega_{r1}$, the contribution to the irradiance on the solar cell is calculated as

$$\begin{aligned} dG_{refl} &= \frac{\rho_1}{\pi} G_{hemi(r1)}(\mathbf{r_1} \cdot \mathbf{n_c}) d\Omega_{r1} \\ &= \rho_1 G_{hemi(r1)} dF_{c \to r1} \end{aligned} \tag{9}$$

where ρ_1 and $G_{hemi(r1)}$ are the reflectivity and the irradiance of the primary Lambertian reflector intersected by $\mathbf{r_1}$, respectively. The irradiance $G_{hemi(r1)}$ consists of three components: (1) the beam irradiance; (2) the diffuse irradiance; and (3) the reflected irradiance by secondary reflectors (i.e., surfaces intercepted by secondary rays). The first two components can be determined using Equation (2) and Equation (3) from the position of the primary reflector instead of the position of the solar cell. The third component is calculated recursively using Equation (9) from the position of the primary reflector. To limit the recursivity of the problem, the irradiance incident on secondary reflectors ($G_{hemi(r2)}$) is calculated considering only the sky beam and sky diffuse irradiance according to Equation (10).

$$G_{hemi(r2)} = DNI (\mathbf{b} \cdot \mathbf{n_2}) SF + Pz(DHI, SVF) \tag{10}$$

where $\mathbf{n_2}$ is the normal vector to the secondary reflector and Pz is the simplified Perez diffuse irradiance model according to which the diffuse irradiance is calculated as the sum of the circumsolar, horizon band and isotropic background contributions.[7] For each secondary reflector, the shading factor (SF) and the sky view factor (SVF) are calculated from the shadow maps stored in memory.

It should be noted that an intrinsic bias arises in this approach since it is limited to two ray reflections. This means that, even for an ideal simulation where the number of rays tends to infinity, the

simulated irradiance on a specific sensor might differ from the actual irradiance received by the sensor. Assuming a perfect description of the optical properties of the materials in the scene and a perfect description of the sky radiance distribution, the proposed approach should result in an underestimation of the irradiance incident on the sensor. It is also worth noting, that this bias is even larger in view factor models (both 2D and 3D) because most methods described in the literature are equivalent to a ray tracing model limited to a single ray bounce. To compensate this bias in view factor models, the most common practice consists in overestimating the irradiance incident on the ground by considering that unshaded sectors receive the global horizontal irradiance (*GHI*) and shaded sectors receive only the diffuse horizontal irradiance (*DHI*).[16,18-20] The overestimation of irradiance approximately compensates the bias introduced by the limitations of the view factor models. It is possible to apply a similar workaround to the proposed approach by adding a third term to Equation (10) to approximate the reflected light on secondary reflectors considering the local albedo α:

$$
\begin{aligned}
G_{\text{hemi(r2)}} = {} & DNI\,(\mathbf{b}\cdot\mathbf{n_2})\,SF + \\
& Pz(DHI, SVF) + \\
& \alpha\,GHI\,(1-SVF)
\end{aligned}
\tag{11}
$$

Using the ray tracing results, the irradiance incident on the solar cell can be quickly recalculated if the reflectivity of a surface changes. This allows to efficiently simulate surfaces with time-varying reflectivity values by considering $\rho(t)$ in Equation (9). Furthermore, all the presented equations can be expressed as a function of a specific wavelength and later integrated over the relevant spectral range to quickly perform spectrally resolved irradiance simulations. To demonstrate the ability of the proposed approach to perform spectral simulations, in this work the solar spectrum is modelled combining *DNI* and *DHI* spectra generated with the SMARTS model[47-49] and the SBDART model.[50] The *DNI* and *DHI* spectra were originally generated for solar azimuth angles ranging from 0° to 89° in steps of 1°, and then interpolated to calculate the spectral distribution of the beam and diffuse components for different solar altitude values. SBDART was used to generate spectra for 3 different sky conditions (clear, cloudy and overcast) and a *DNI*-based sky classifier was used to identify the sky condition at each time as explained in Appendix D. By contrast, SMARTS can only generate spectra for clear sky conditions, thus it is expected to differ significantly from the actual spectra under partially cloudy and overcast skies. It is worth to note that several studies propose spectral sky models,[51-56] yet more research is needed to develop a generalised model that can accurately describe the spectral sky radiance in the presence of clouds.

Another relevant characteristic of the proposed approach is that it allows to directly simulate the effect of the incidence angle modifier (IAM) and the transmissivity of the PV module front layer.[57] Since the direction of all the irradiance contributions is known, the angular effects can be easily included by adding a multiplicative factor in Equations (2), (3) and (5).

4 | EXPERIMENTAL VALIDATION

4.1 | Measurement setup

The irradiance model described in Section 3, was implemented and validated using measurements taken at the PVMD monitoring station shown in Figure 4A located in Delft, the Netherlands. At the monitoring station, a Kipp & Zonen SOLYS2 sun tracker equipped with a SMP 21 pyranometer and a SHP1 pyrheliometer was used to measure the diffuse horizontal irradiance (*DHI*) and the direct normal irradiance (*DNI*), respectively. The three irradiance sensors indicated in Figure 4B were used to validate the model: a monocrystalline ISET sensor (IKS Photovoltaik) facing South and tilted 30° (S1); a SMP10 thermopile pyranometer (Kipp & Zonen) facing 65° East from North and tilted 90° (S2); and a MS-700 spectroradiometer (EKO Instruments) mounted horizontally (S3).

The 3D model of the monitoring station shown in Figure 4B was generated to simulate the irradiance at the position of sensors S1, S2 and S3. The 3D model was created combining information from floor plans, Lidar data and in-situ measurements with a laser distance meter. The accuracy of the 3D model was further evaluated by comparing photographs taken with an Horicatcher device at 10 positions with raster images generated from the 3D model. The relative difference in the sky view factor between the photographs and the raster images is below 2% for all the positions evaluated. Rasterised images generated with the implemented ray tracer from the perspective of the three sensors are presented in Appendix A.
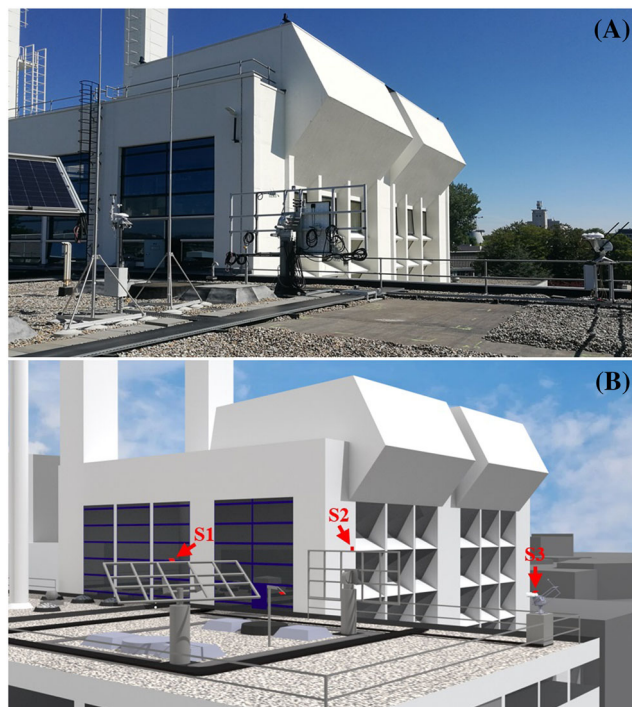
FIGURE 4 PVMD monitoring station. (A) Photograph. (B) Ray tracing-based rendering generated with the CAD model
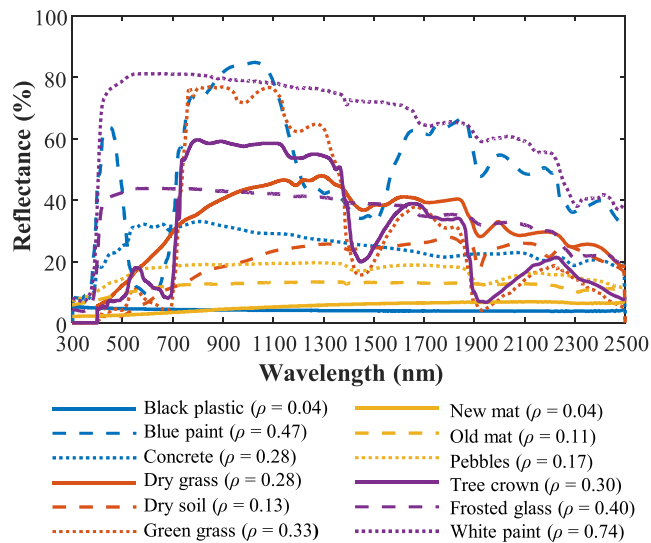
FIGURE 5 Spectral reflectivity of the surfaces in the scene. The weighted average reflectivity of each material considering the AM1.5G solar spectrum is indicated in the legend in between parentheses

All the surfaces in the scene are either ideal specular or Lambertian reflectors. Samples of most surfaces in the scene were taken and characterised using a LAMBDA 1050 spectrophotometer. The spectral reflectance of the surrounding vegetation and the concrete was retrieved from the ECOSTRESS Spectral Library.[58,59] The spectral and average reflectivity of all the materials in the scene is presented in Figure 5.

4.2 | Simulation parameters

The irradiance calculated with the proposed approach was compared to measurements and to simulations performed with *Radiance* (using the program *rtrace*), a well-established lighting simulation software described in Appendix B. The selection of the input parameters for *rtrace* is crucial to obtain accurate results and reasonable computation times. Considering the size and the level of detail of the scene the following values were chosen: $ad = 1024$, $as = 64$, $ab = 2$, $aa = 0.1$, $ar = 1024$.

The effect of the ambient bounces (*ab*) in the simulated irradiance on sensor S2 is shown in Figure 6 using *DNI* and *DHI* minutely measured during 21 August 2020, as inputs to calculate the sky radiance distribution. As already explained, higher *ab* improves the accuracy of the simulation; however, doubling the value of *ab* approximately doubles the computation time. Due to the highly reflective white wall ($\rho = 0.74$) in front of the sensor, it is clear that more than one ambient bounce is required to obtain reasonable results. The normalised[‡] mean bias errors (nMBE) and root square errors (nRMSE) are given in Table 1. As expected, results converge when the number of ambient
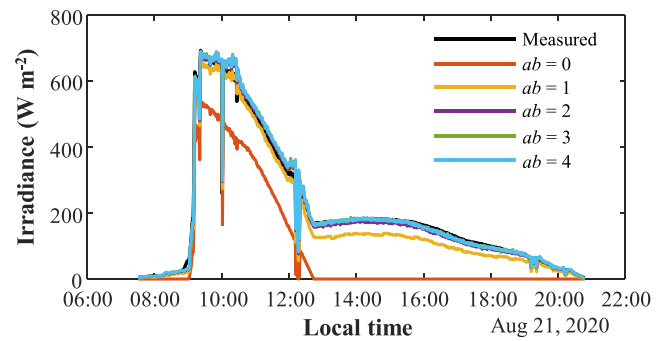
FIGURE 6 Effect of the ambient bounces (*ab*) parameter on the simulated irradiance on sensor S2 with *Radiance*. The simulation with *ab* = 0 only calculates the beam irradiance incident on the sensor

bounces is increased. In this scenario, the most accurate simulation (*ab* = 4) overestimates the daily irradiation by 2% as indicated by the nMBE value in Table 1. Results also indicate that using more than three ambient bounces offers no improvement in the simulation accuracy, yet it significantly increases the total computation time. Nevertheless, for the simulation presented in the following section the ambient bounces were limited to 2, since this *ab* value offered the most reasonable compromise between accuracy and computation time.

To make a fair comparison between the proposed approach and *Radiance*, the number of rays in both models must be similar. The simulation results of the proposed approach presented in the following sections were obtained using an equiangular discretisation (Figure 2B) with 60 azimuthal and 30 polar divisions. Hence, when hemispherical sampling is performed, 900 rays are cast with the proposed approach compared to the *ad* value of 1024 typically employed in *Radiance*.

When using the proposed approach, the results of the ray tracing calculations for each of the simulated sensors were stored in memory to accelerate the irradiance calculations. Ray tracing results include the indices of the primary and secondary rays that intersect with the scene, the normal vectors and the optical properties of the intersected surfaces, and the shadow maps. The simulations results with 900 primary rays occupied only 5gb in average per each evaluated test point. Consequently, the ray tracing results of a 72-cell PV module with 4 test points per cell in a complex scenario would occupy less than 1.5 GB of storage space.

4.3 | Irradiation simulations

The irradiance incident on sensors S1 and S2 was simulated using minutely *DNI* and *DHI* measurements taken between August 2020 and February 2021. A comparison between the proposed approach and *Radiance* was carried out considering the average reflectivity values for the surfaces listed in Figure 5.

The incidence angle modifier (IAM) of reference cell S1 was modelled according to the physical model presented in De Soto et al[60]

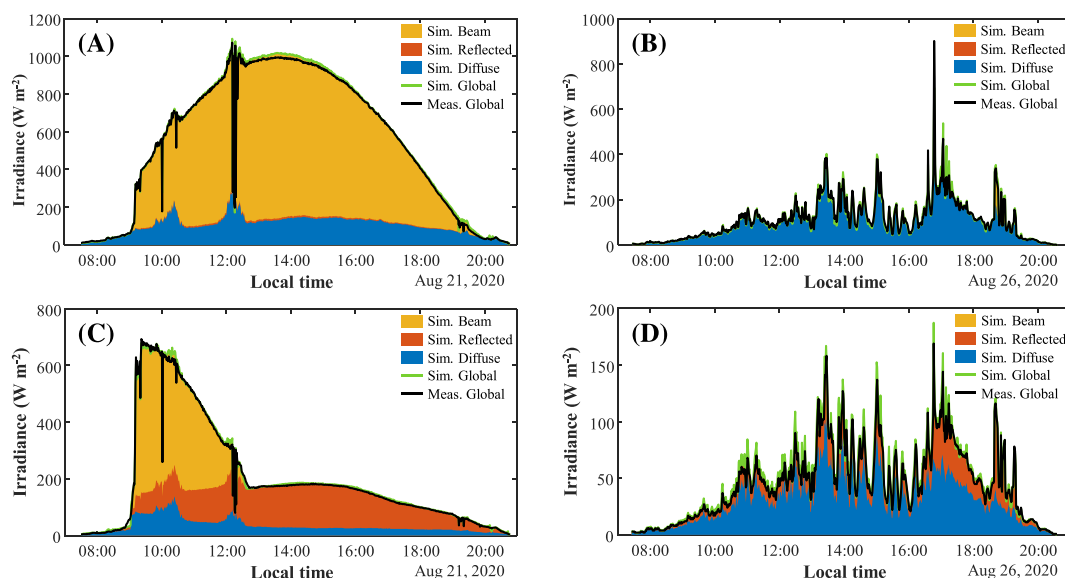[‡]Errors are normalised by the mean irradiance value.

since manufacturer data were not available. In the proposed approach, the calculation of the IAM for the radiance incident on the solar cell from each direction is straightforward, as explained in Section 3.2. On the other hand, *rtrace* does not inform the angular distribution of the incident radiance. Hence, to improve the simulation of the IAM effect, the diffuse and reflected components were separated from the beam component by performing simulations with 0 and 2 ambient bounces. Then, the angle of incidence of the beam component was calculated as in Equation (2), and the effective angle of incidence of the reflected and diffuse components (56.8°) was calculated according to Gilman et al.[61]

In Figure 7, the irradiance simulated with the proposed approach is compared to the measurements of sensors S1 and S2 in clear sky and overcast conditions. The simulated global irradiance was decomposed into its three components. The reflected irradiance component on sensor S1 is almost negligible due to the low tilt of the sensor. Contrarily, the reflected component has a significant contribution on the global irradiance received by sensor S2, which is oriented vertically and in close proximity to a highly reflective white wall. This effect is more evident during the afternoon of the clear sky day

(21 August 2020), when the sun is behind the sensor and the white wall is directly illuminated.

The proposed approach is compared to *Radiance* and the measurements in Figure 8, where it is possible to see that both models
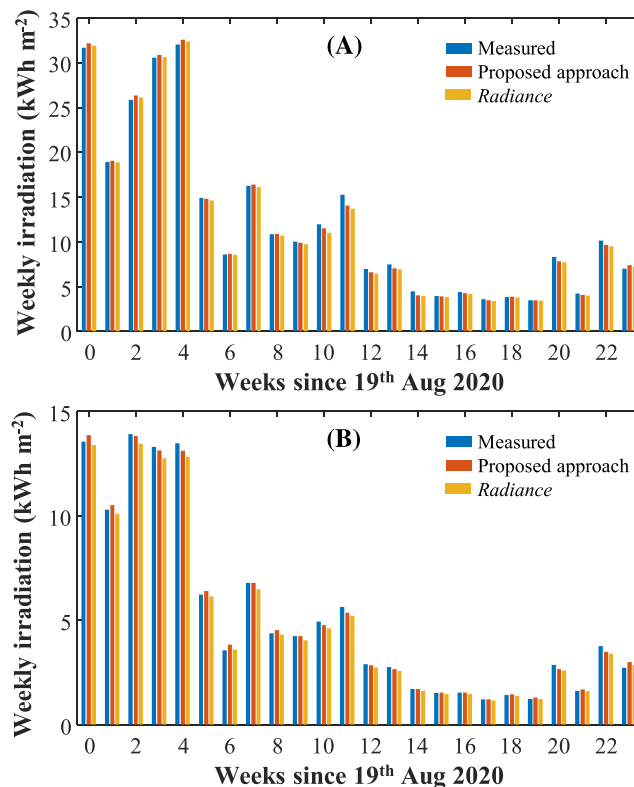
FIGURE 8 Comparison between the measured and simulated weekly irradiation on reference cell S1 (A) and pyranometer S2 (B)

TABLE 1 Normalised mean bias error, mean absolute error and root mean square error corresponding to Figure 6

ab	0	1	2	3	4
nMBE (%)	58.0	12.3	0.3	−2.0	−2.1
nMAE (%)	58.0	12.4	4.1	3.9	4.0
nRMSE (%)	65.1	14.5	5.6	6.3	6.3

Note: Values are normalised by the mean of the measured data and negative nMBE values indicate that the simulation overestimates the irradiance.

FIGURE 7 Simulated irradiance components on sensors S1 and S2 with the proposed approach. (A) Measured and simulated irradiance on sensor S1 during a clear sky day. (B) Measured and simulated irradiance on sensor S1 during an overcast day. (C) Measured and simulated irradiance on sensor S2 during a clear sky day. (D) Measured and simulated irradiance on sensor S2 during an overcast day

can accurately simulate the weekly irradiation throughout the entire period. The irradiation was calculated by integrating the minutely irradiance over an entire week after filtering out the outliers (0.2% of the data points). The relative mean absolute error in the daily irradiation simulated with the proposed approach is 3.5% and 4.3% for sensors S1 and S2, respectively. The normalised errors calculated based on the minutely measurements are presented in Table 2. The simulated

TABLE 2 Normalised mean bias error, mean absolute error and root mean square error of the simulated irradiance on sensors S1 and S2 between 19 August 2020 and 5 February 2021

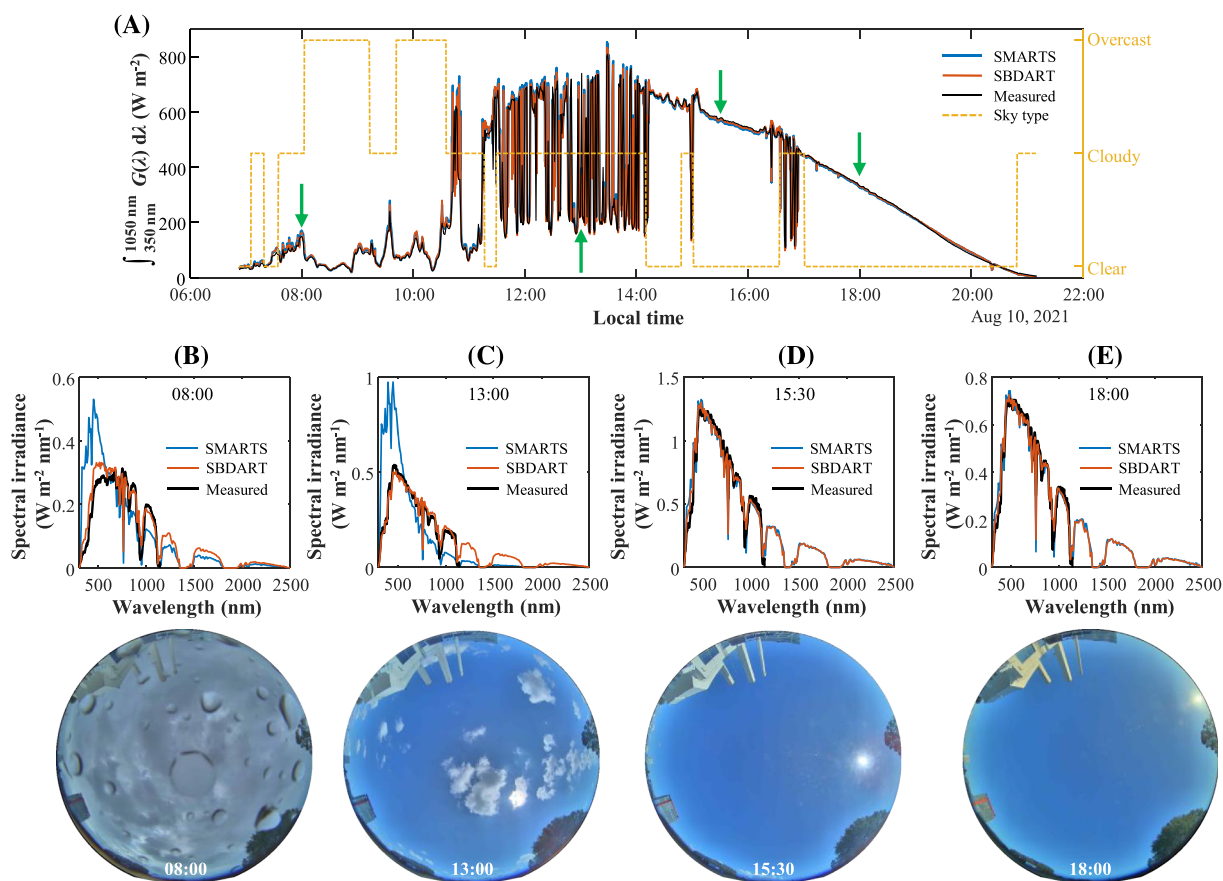| Sensor	Proposed approach		Radiance	
	S1	S2	S1	S2
nMBE (%)	0.1	-0.1	1.4	3.4
nMAE (%)	7.7	8.1	7.2	7.6
nRMSE (%)	21.1	12.7	21.5	12.9

Note: Values are normalised by the mean of the measured data and negative nMBE values indicate that the simulation overestimates the irradiance.

irradiance on sensor S1 is more accurate with the proposed approach than with *Radiance* mainly due to the approximation of the effective angle of incidence of the diffuse irradiance component. Despite the fact that reference cells tend to underestimate the measured irradiance in cloudy skies and low solar altitudes as a result of the spectral response of silicon,[62] the simulated irradiances on reference cell S1 present lower nMAE compared to pyranometer S2. The reason is because sensor S1 receives much less reflected irradiance than sensor S2. It can also be noticed, especially in Figure 8B, that the proposed approach tends to yield higher values than *Radiance*. In part, this is because the proposed approach considers the contribution of the reflected irradiance on secondary reflectors expressed in Equation (11). If this contribution is neglected and Equation (10) is used instead, the nMBE of the proposed approach at sensor S2 increases to 0.5%. On the other hand, the high nRMSE of sensor S1 is explained by the large response time difference between the reference cell S1 ($\tau_{95\%} < 100ms$) and the thermopile sensors that measure DNI and DHI ($\tau_{95\%} < 2s$). Especially during partially cloudy day when illumination conditions are varying quickly, the difference in response time leads to an increased RMSE.

FIGURE 9 Spectral irradiance simulations with the proposed approach. (A) Integrated measured and simulated spectral irradiance on sensor S3. The green arrows indicate the time instants at which the spectra are compared. The yellow dashed line indicates which SBDART spectra was chosen at each time according to the simple sky classifier in Appendix D. (B–D) Spectra and sky images at 8:00 a.m. 1:00 p.m., 3:30 p.m. and 6:00 p.m., respectively

4.4 | Spectral simulations

To demonstrate the ability of the proposed approach to perform spectrally resolved simulations, the measured and simulated irradiance at the position of spectroradiometer S3 are compared in Figure 9 during an entire day. The irradiance was simulated with 5nm resolution between 300 and 2500 nm, using *DNI* and *DHI* measurements to scale the spectra generated with SMARTS and SBDART(refer to Tables 3 and 4). The time resolution for the spectral simulations was 30 s. Using the precalculated ray tracing solution at the position of S3, it took approximately 3 min to evaluate the spectral irradiance for an entire day.

The irradiance in Figure 9A is integrated between 350 and 1050 nm, which is the valid measurement range of S3. It should be

TABLE 3 SMARTS parameters

Parameter	Value
Surf. Pressure (mb)	1013.25
Altitude (km)	0
Atmosphere	U.S. Std Atm 1976
Water vapoUr	From ref. atm. and alt.
Ozone	Def. ref. atm.
CO2 (ppvm)	370
Ext. Spectrum	Gueymard 2002
Aerosol model	Urban S&F
Turbidity at 500 nm	0.084
Albedo	Light soil
Spectral range (nm)	280–4000
Circumsolar	Radiometer aperture 2.9

TABLE 4 SBDART parameters

Parameter	Clear	Cloudy	Overcast
NF	1	1	1
ISAT	0	0	0
WLINF	0.28	0.28	0.28
WLSUP	4	4	4
WLINC	0.001	0.001	0.001
SZA	0:89.5	0:89.5	0:89.5
ISALB	6	6	6
IDATM	6	6	6
UW	1.42	1.42	1.42
UO3	0.324	0.324	0.324
IAER	1	1	1
TBAER	0.084	0.084	0.084
ZCLOUD	n/a	2.0	2.0 −6.0
TCLOUD	n/a	1.0	60.0 60.0
NRE	n/a	10.0	20.0 20.0
ZOUT	0,1	0,1	0,1
IOUT	1	1	1

noticed, that this wavelength range concentrates approximately 77.5% of the power in the AM1.5G spectrum and covers the most significant part of the spectral responsivity of any PV module on the market. The sky camera pictures in Figure 9 show that during the morning it was rainy and the sky was overcast. Towards the afternoon, the clouds were dispersed and the sky became clear. Overall, the simulated integral irradiance is in good agreement with the measurements. The largest deviations from the measurements occur when the sun is covered by clouds.

In particular, the comparison between the measurements and the simulations using SMARTS spectra as input (Figure 9B) shows a significant spectral mismatch in the morning. This mismatch was expected since clouds cause a red-shift in the spectrum[51] and SMARTS can only be used to generate spectra for clear sky days. It can also be noted that, as clouds disappear in Figure 9D,E, the spectral match improves for exactly the same reasons.

As expected, in the presence of clouds, the results of the simulations using SBDART spectra are in better agreement with the measurements compared to SMARTS. However, the spectral mismatch at 8 a.m. illustrates the challenge of generalising cloudy and overcast spectra. Spectral matching in the presence of clouds could be improved by defining new sky types and using additional inputs to the sky classifier algorithm to identify each sky type.

These results show that the proposed approach is able to perform simulations with high spectral and temporal resolution. Nevertheless, it is also evident the importance of using a proper sky model to describe the effect of clouds.

5 | CONCLUSIONS

A model for simulating the irradiance incident on PV systems in geometrically complex scenes has been presented. The model is a backward ray tracer limited to two ray bounces, which only considers ideally diffuse and specular reflectors to simplify the calculation of interreflections.

The main advantage of the presented simulation approach is that it allows to fully decouple the solution of the ray tracing problem from both the optical properties (i.e., reflectivity) of the surfaces in the scene and the illumination conditions. The decoupling of the irradiance simulation problem into three parts allows to significantly reduce computation times in comparison to conventional ray tracing simulation approaches. The highly time consuming ray tracing simulations only need to be solved once and the results are stored in memory to quickly evaluate the irradiance profile on the module. Moreover, with the presented approach, it is possible to solve problems that could otherwise imply a very long computation time, e.g., solving the irradiance incident on a PV module with high spectral resolution (over 100 spectral bands) at every minute during an entire year.

A validation study was carried out using measurements of different types of irradiance sensors installed at the PVMD monitoring station, in the Netherlands. A detailed 3D description of the monitoring station was created to simulate the irradiance incident on the sensors.

It was determined that the mean absolute error of the daily irradiation simulated with the proposed approach over a period of 6 months is lower than 5% using both a pyranometer and a reference cell. A comparison with *Radiance* limited to two ambient bounces, suggests that the optical performance of the proposed approach is slightly better and the computation time can be reduced by three orders of magnitude when performing annual irradiance simulations with minutely resolution.

Finally, spectral simulations were performed using the diffuse and beam spectra generated with SMARTS and SBDART as inputs to the irradiance model, and compared to measurements taken with a spectroradiometer. Results indicate that even though the proposed approach is capable of quickly computing the incident irradiance with high spectral and temporal resolution, the simulated spectrum can significantly differ from the measurements. While under clear sky conditions there is a good agreement between measurements and simulations, in the presence of clouds there is a larger mismatch due to the a red-shift in the spectrum in comparison to clear sky conditions. The presented results put in evidence the need for a more sophisticated spectral sky model to reproduce the atmospheric conditions and account for the effect of clouds.

The ability of the proposed irradiance simulation approach to distinguish between different types of reflectors instead of using a single albedo value allows to improve the accuracy of the estimation of the irradiance impinging on PV modules that receive a large portion of reflected irradiance. Moreover, in comparison to traditional ray tracers, the presented approach offers a practical way to simulate surfaces with time varying optical properties and compute the spectral irradiance incident on a PV module. These features are particularly valuable for the simulation of bifacial and tandem PV systems.

ACKNOWLEDGEMENT

ORCID

Calcabrini Andres https://orcid.org/0000-0002-1940-4705
Manganiello Patrizio https://orcid.org/0000-0002-4752-0068

REFERENCES

1. Ballif C, Perret-Aebi L-E, Lufkin S, Rey E. Integrated thinking for photovoltaics in buildings. *Nat Energy*. 2018;3(6):438-442.
2. Ortiz Lizcano JC, Haghighi Z, Wapperom S, Infante Ferreira C, Isabella O, vd Dobbelsteen A, Zeman M. Photovoltaic chimney: thermal modeling and concept demonstration for integration in buildings. *Prog Photovolt: Res Appli*. 2020;28(6):465-482.
3. Brito MC, Santos T, Moura F, Pera D, Rocha J. Urban solar potential for vehicle integrated photovoltaics. *Trans Res Part D: Transp Environ*. 2021;94:102810.
4. Kutter C, Basler F, Alanis LE, Markert J, Heinrich M, Neuhaus DH. Integrated lightweight, glass-free pv module technology for box bodies of commercial trucks. In: 37th European PV Solar Energy Conference and Exhibition (EUPVSEC); 2020:1711-1718.
5. United Nations. Sustainable development goals. https://www.un.org/sustainabledevelopment/energy/; 2016.
6. Liu BenjaminYH, Jordan RC. The long-term average performance of flat-plate solar-energy collectors: with design data for the us, its outlying possessions and canada. *Sol Energy*. 1963;7(2):53-74.
7. Perez R, Seals R, Ineichen P, Stewart R, Menicucci D. A new simplified version of the Perez diffuse irradiance model for tilted surfaces. *Sol Energy*. 1987;39(3):221-231.
8. Reindl DT, Beckman WA, Duffie JA. Evaluation of hourly tilted surface radiation models. *Sol Energy*. 1990;45(1):9-17.
9. Freeman J, Freestate D, Hobbs W, Riley C. Using measured plane-of-array data directly in photovoltaic modeling: methodology and validation. In: 2016 IEEE 43rd Photovoltaic Specialists Conference (PVSC) IEEE; 2016:2653-2656.
10. Khalil SA, Shaffie AM. Evaluation of transposition models of solar irradiance over egypt. *Renew Sustain Energy Rev*. 2016;66:105-119.
11. Mubarak R, Hofmann M, Riechelmann S, Seckmeyer G. Comparison of modelled and measured tilted solar irradiance for photovoltaic applications. *Energies*. 2017;10(11):1688.
12. Ineichen P, Guisan O, Perez R. Ground-reflected radiation and albedo. *Sol Energy*. 1990;44(4):207-214.
13. Jäger K, Tillmann P, Becker C. Detailed illumination model for bifacial solar cells. *Opt Express*. 2020;28(4):4751-4762.
14. Mermoud A, Wittmer B. Bifacial shed simulation with PVSyst. In: Bifacial workshop; 2017:25-26.
15. Marion B, MacAlpine S, Deline C, et al. A practical irradiance model for bifacial PV modules. In: 2017 IEEE 44th Photovoltaic Specialist Conference (PVSC) IEEE; 2017:1537-1542.
16. Chudinzow D, Haas J, Díaz-Ferrán G, Moreno-Leiva S, Eltrop L. Simulating the energy yield of a bifacial photovoltaic power plant. *Solar Energy*. 2019;183:812-822.
17. Hansen CW, Gooding R, Guay N, et al. A detailed model of rear-side irradiance for bifacial pv modules. In: 2017 IEEE 44th Photovoltaic Specialist Conference (PVSC) IEEE; 2017:1543-1548.
18. Shoukry I, Libal J, Kopecek R, Wefringhaus E, Werner J. Modelling of bifacial gain for stand-alone and in-field installed bifacial PV modules. *Energy Procedia*. 2016;92:600-608.
19. Yusufoglu UA, Pletzer TM, Koduvelikulathu LJ, Comparotto C, Kopecek R, Kurz H. Analysis of the annual performance of bifacial modules and optimization methods. *IEEE J Photovoltaics*. 2014;5(1):320-328.
20. Berrian D, Libal J. A comparison of ray tracing and view factor simulations of locally resolved rear irradiance with the experimental values. *Prog Photovolt Res Appl*. 2020;28(6):609-620.
21. Nussbaumer H, Janssen G, Berrian D, et al. Accuracy of simulated data for bifacial systems with varying tilt angles and share of diffuse radiation. *Solar Energy*. 2020;197:6-21.
22. Gross U, Spindler K, Hahne E. Shapefactor-equations for radiation heat transfer between plane rectangular surfaces of arbitrary position and size with parallel boundaries. *Lett Heat Mass Transf*. 1981;8(3):219-227.
23. Sönmez FF, Ziar H, Isabella O, Zeman M. Fast and accurate ray-casting-based view factor estimation method for complex geometries. *Sol Energy Mater Sol Cells*. 2019;200:109934.
24. Bartell F, Dereniak E, Wolfe W. The theory and measurement of bidirectional reflectance distribution function (BRDF) and bidirectional transmittance distribution function (BTDF). In: Radiation scattering in optical systems, Vol. 257 International Society for Optics and Photonics; 1981:154-160.
25. Santbergen R, Muthukumar VA, Valckenborg RME, van de Wall WJA, Smets AHM, Zeman M. Calculation of irradiance distribution on PV modules by combining sky and sensitivity maps. *Sol Energy*. 2017; 150:49-54.
26. Holst H, Winter M, Vogt MR, Bothe K, Köntges M, Brendel R, Altermatt PP. Application of a new ray tracing framework to the analysis of extended regions in SI solar cell modules. *Energy Procedia*. 2013;38:86-93. https://www.daidalos-cloud.de

27. PV Lighthouse. Sunsolve. https://www.pvlighthouse.com.au/sunsolve; 2021.

28. Santbergen R, Meguro T, Suezaki T, Koizumi G, Yamamoto K, Zeman M. Genpro4 optical model for solar cell simulation and its application to multijunction solar cells. *IEEE J Photovoltaics*. 2017;7(3):919-926. https://asa.ewi.tudelft.nl/

29. Ward GJ. The radiance lighting simulation and rendering system. In: Proceedings of the 21st Annual Conference On Computer Graphics and Interactive Techniques; 1994:459-472.

30. Deline C, Ayala S. Bifacial_Radiance. computer software. USDOE Office of Energy Efficiency and Renewable Energy (EERE), Solar Energy Technologies Office (EE-4S) 10.11578/dc.20180530. 16. [Online]. Available: https://github.com/NREL/bifacial_radiance; 2021.

31. Hansen CW, Stein JS, Deline C, MacAlpine S, Marion B, Asgharzadeh A, Toor F. Analysis of irradiance models for bifacial PV modules. In: IEEE 43rd Photovoltaic Specialists Conference (PVSC) IEEE; 2016:138-0143.

32. Horvath I, Manganiello P, Goverde H, et al. Towards efficient and accurate energy yield modelling of bifacial PV systems. In: 35th European pv Solar Energy Conference and Exhibition (EUPVSEC); 2018.

33. Pelaez SA, Deline C, Greenberg P, Stein JS, Kostuk RK. Model and validation of single-axis tracking with bifacial PV. *IEEE J Photovoltaics*. 2019;9(3):715-721.

34. Pelaez SA, Deline C, MacAlpine SM, Marion B, Stein JS, Kostuk RK. Comparison of bifacial solar irradiance model predictions with field validation. *IEEE J Photovoltaics*. 2018;9(1):82-88.

35. Tregenza PR, Waters IM. Daylight coefficients. *Light Res Technol*. 1983;15(2):65-71.

36. Reinhart CF, Walkenhorst O. Validation of dynamic radiance-based daylight simulations for a test office with external blinds. *Energy Build*. 2001;33(7):683-697.

37. Brennan MP, Abramase AL, Andrews RW, Pearce JM. Effects of spectral albedo on solar photovoltaic devices. *Sol Energy Mater Sol Cells*. 2014;124:111-116.

38. Monokroussos C, Gao Q, Zhang X, et al. Rear-side spectral irradiance at 1 sun and application to bifacial module power rating. *Prog Photovolt Res Appl*. 2020;28(8):755-766.

39. Ziar H, Sönmez FF, Isabella O, Zeman M. A comprehensive albedo model for solar energy applications: geometric spectral albedo. *Appl Energy*. 2019;255:113867.

40. Hörantner MT, Snaith HJ. Predicting and optimising the energy yield of perovskite-on-silicon tandem solar cells under real world conditions. *Energy Environ Sci*. 2017;10(9):1983-1993.

41. Lindsay N, Libois Q, Badosa J, Migan-Dubois A, Bourdin V. Errors in pv power modelling due to the lack of spectral and angular details of solar irradiance inputs. *Sol Energy*. 2020;197:266-278.

42. Gul M, Kotak Y, Muneer T, Ivanova S. Enhancement of albedo for solar energy gain with particular emphasis on overcast skies. *Energies*. 2018;11(11):2881.

43. Riedel-Lyngskær N, Ribaconka M, Pó M, Thorsteinsson S, Thorseth A, Dam-Hansen C, Jakobsen ML. Spectral albedo in bifacial photovoltaic modeling: what can be learned from onsite measurements?. In: 2021 48th IEEE Photovoltaic Specialists Conference (PVSC) IEEE; 2021:1335-1338.

44. Ward G, Shakespeare R. Rendering with radiance: the art and science of lighting visualization. *Calculation Methods*. 3rd ed.; 1998:491-562.

45. Möller T, Trumbore B. Fast, minimum storage ray-triangle intersection. *J Graph Tools*. 1997;2(1):21-28.

46. Perez R, Seals R, Michalsky J. All-weather model for sky luminance distribution–preliminary configuration and validation. *Solar Energy*. 1993;50(3):235-245.

47. Gueymard C. Smarts2, a simple model of the atmospheric radiative transfer of sunshine: algorithms and performance assessment. FSEC-PF-270-95, Florida Solar Energy Center Cocoa, FL; 1995.

48. Gueymard CA. Parameterized transmittance model for direct beam and circumsolar spectral irradiance. *Solar Energy*. 2001;71(5):325-346.

49. Gueymard CA, Myers D, Emery K. Proposed reference irradiance spectra for solar energy systems testing. *Solar Energy*. 2002;73(6):443-467.

50. Ricchiazzi P, Yang S, Gautier C, Sowle D. Sbdart: a research and teaching software tool for plane-parallel radiative transfer in the Earth's atmosphere. *Bull Am Meteorol Soc*. 1998;79(10):2101-2114.

51. Bartlett JS, Ciotti AM, Davis RF, Cullen JJ. The spectral effects of clouds on solar irradiance. *J Geophys Res Oceans*. 1998;103(C13):31017-31031.

52. Bird RE, Riordan C. Simple solar spectral model for direct and diffuse irradiance on horizontal and tilted planes at the Earth's surface for cloudless atmospheres. *J Appl Meteorol Climatol*. 1986;25(1):87-97.

53. Ernst M, Holst H, Winter M, Altermatt PP. Suncalculator: a program to calculate the angular and spectral distribution of direct and diffuse solar radiation. *Sol Energy Mater Sol Cells*. 2016;157:913-922.

54. Hosek L, Wilkie A. An analytic model for full spectral sky-dome radiance. *ACM Trans Graph (TOG)*. 2012;31(4):1-9.

55. Kider Jr JT, Knowlton D, Newlin J, Li YK, Greenberg DP. A framework for the experimental comparison of solar and skydome illumination. *ACM Trans Graph (TOG)*. 2014;33(6):1-12.

56. Winter M, Holst H, Vogt MR, Altermatt PP. Impact of realistic illumination on optical losses in SI solar cell modules compared to standard testing conditions. In: 31st European PV Solar Energy Conference and Exhibition (EUPVSEC); 2015:1869-1874.

57. Boppana S, Passow K, Sorensen J, King BH, Robinson C. Impact of uncertainty in IAM measurement on energy predictions. In: 2018 IEEE 7th World Conference on Photovoltaic Energy Conversion (WCPEC)(a Joint Conference of 45th IEEE PVSC, 28th PVSEC & 34th eu pvsec) IEEE; 2018:2276-2281.

58. Baldridge AM, Hook SJ, Grove CI, Rivera G. The aster spectral library version 2.0. *Remote Sens Environ*. 2009;113(4):711-715.

59. Meerdink SK, Hook SJ, Roberts DA, Abbott EA. The ecostress spectral library version 1.0. *Remote Sens Environ*. 2019;230:111196.

60. De Soto W, Klein SA, Beckman WA. Improvement and validation of a model for photovoltaic array performance. *Sol Energy*. 2006;80(1):78-88.

61. Gilman P, Dobos A, DiOrio N, Freeman J, Janzou S, Ryberg D. Sam photovoltaic model technical reference update. NREL/TP-6A20-67399, Golden, CO, USA, NREL; 2018.

62. Karki S, Ziar H, Korevaar M, Bergmans T, Mes J, Isabella O. Performance evaluation of silicon-based irradiance sensors versus thermopile pyranometer. *IEEE J Photovoltaics*. 2020;11(1):144-149.

63. Cook RL. Stochastic sampling in computer graphics. *ACM Trans Graph (TOG)*. 1986;5(1):51-72.

64. Subramaniam S. Daylighting simulations with radiance using matrix-based methods. Lawrence Berkeley National Laboratory; 2017.

65. Ward GJ, Rubinstein FM, Clear RD. A ray tracing solution for diffuse interreflection. In: Proceedings of the 15th Annual Conference on Computer Graphics and Interactive Techniques; 1988:85-92.

APPENDIX A: VIEW FROM ANALYSED SENSORS
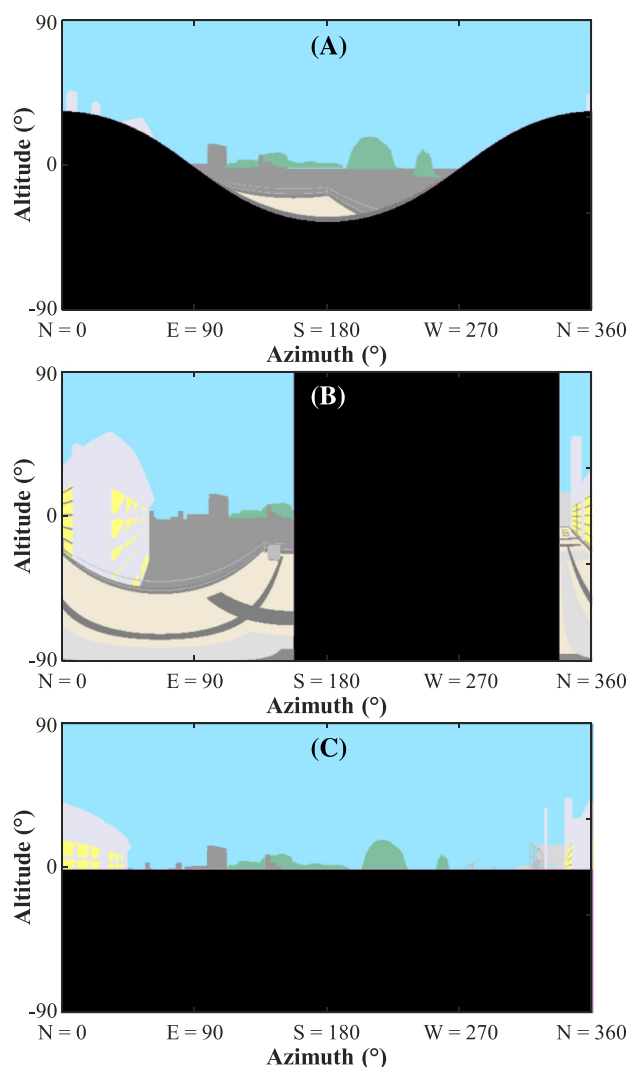
FIGURE A1 Raster images generated with our ray tracer depicting the field view from the perspective of the irradiance sensors. The black regions in the rasters correspond to the hemisphere behind the plane of array of the sensors. (A) View from reference cell S1 tilted 31° and facing South. (B) View from pyranometer S2 tilted 90° and facing 65° East from North (approximately North-Northeast). (C) View from spectroradiometer S3 installed horizontally

APPENDIX B: IRRADIANCE SIMULATIONS WITH RADIANCE

Radiance[44] is a highly flexible and optimised lighting simulation tool that has been continuously improved and validated over the last three decades. There are several programs that form part of this software suite. The program *rtrace* is used to trace the rays through the scene and calculate the irradiance on the solar cells. It is relevant to highlight the similarities and differences between *Radiance* and the proposed approach.

In order to perform a ray tracing simulation with *rtrace*, the illumination conditions (i.e., *DNI*, *DHI* and the solar position) must be specified to generate a description of the light sources with the program *gendaylit*. In *Radiance*, direct and diffuse light sources are sampled separately.[44] The sun is considered a directional point light source and it is sampled with a single deterministic ray. The sky dome is considered an extended diffuse light source described by Perez model,[46] and it is sampled stochastically. The stochastic sampling approach, in opposition to the proposed deterministic sampling, allows to eliminate aliasing artefacts in image rendering.[63] Furthermore, *Radiance* can simulate surfaces with arbitrary *BSDF* functions, not only ideally diffuse and specular reflectors as in the proposed approach. The density of sampling rays can be adapted according to the illumination conditions to refine the sampling in in regions with larger irradiance gradients. Hence, when the program *rtrace* is used to calculate irradiance, the ray tracing simulations must be repeated for every time step and
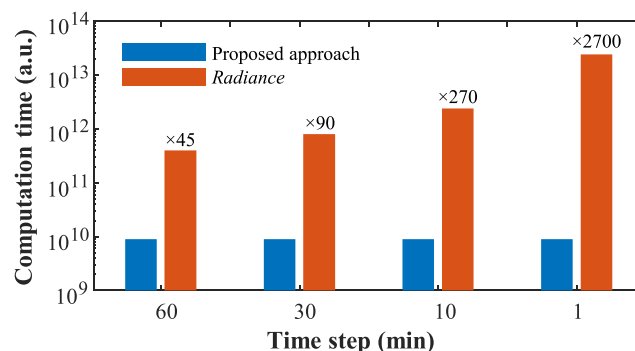
FIGURE B1 Relative computation time of year-long simulations of a 72-cell PV module considering 2 ambient bounces with different temporal resolutions. It is assumed that the computation time is proportional to the number of traced rays according to Appendix B

sky condition. Alternatively, the program *rfluxmtx* in *Radiance*, can be used to calculate daylight coefficients,[64] but this program was not used for this study.

The calculation of diffuse interreflections in *Radiance* is not limited to two ray bounces as in the proposed approach. A user-defined parameter is used to set the maximum number of ray bounces. Moreover, ray tracing calculation are accelerated using the irradiance caching algorithm,[65] which significantly reduces the number of points where higher order hemispherical sampling is performed. Irradiance caching is based on the assumption that diffuse illumination varies slowly over the scene, and hence it is not always necessary to initiate a new hemispherical sampling at each intersection point between a sampling ray and the scene. Under certain conditions, the irradiance at the new sampling point can be interpolated from cached values using irradiance gradients. The user can control the radius of validity of the gradient-based interpolation with different input parameters.

The most relevant *rtrace* parameters for PV simulations are:

- Ambient divisions (*ad*): It indicates the number of primary rays used for hemispherical sampling.
- Ambient super-samples (*as*): It indicates the number of additional sample rays used in ambient divisions that present high variance.
- Ambient bounces (*ab*): It limits the maximum number of ray bounces allowed in the calculation of interreflections.
- Ambient accuracy (*aa*): There is an associated error that is estimated for each point where the irradiance is interpolated using irradiance gradients. If the interpolation error is larger than the ambient accuracy parameter, interpolation cannot be used and a new hemispherical sampling is initiated.
- Ambient resolution (*ar*): it determines the minimum distance between ambient sampling points. When the distance between two sampling points is smaller than the maximum scene dimension multiplied by *aa* and divided by *ar*, the new ambient value is interpolated from the irradiance gradient independently of the error associated with the interpolation.

One major difference between using *rtrace* and the proposed approach is the computation time. The program *rtrace* must be executed one time per simulated time instant; hence, the total computation time increases linearly with the number of simulated time instants. On the contrary, the total computation time with the proposed approach is almost independent of the number of simulated instants. A comparison considering year-long simulations of a 72-cell PV module with different temporal resolutions is presented in Figure B1. The proposed approach is about 45 times faster than *Radiance* at calculating the hourly irradiance, and about 2700 times faster at performing year-long simulations with minutely resolution.

Another important aspect is that the proposed approach can easily handle dozens of spectral bands. However, *Radiance* is limited to only three independent channels (denominated R, G, and B) to calculate spectral irradiance. These channels can be used to perform spectral simulations using three arbitrary spectral bands, not necessarily in the visible spectrum. As a result, when using *Radiance*, ray tracing simulations must be repeated to evaluate the spectral irradiance with more bands.

APPENDIX C: COMPUTATION COMPLEXITY COMPARISON

The total computation time of ray tracing irradiance models is mainly determined by the total number of cast rays.

In *Radiance*, the irradiance caching algorithm limits the geometric growth of the number of samplings required to solve diffuse interreflections. Assuming that in average, the irradiance caching algorithm allows to reduce the number of sampling required at each higher level by 50%,[44] the total number of rays that are traced in one execution of the program *rtrace* when $ab = 2$ is approximately:

$$R_1 = r + \frac{r^2}{2} + \frac{r^3}{8} \tag{C1}$$

where *r* is the original number of sampling rays (i.e., primary rays). The irradiance caching algorithm is particularly effective to evaluate the irradiance on multiple test points, thus R_1 is assumed to be independent of the number of evaluated test points. Nevertheless, since *rtrace* must be executed once per simulated time instant, the total number of traced rays and thus the total computation, time increase linearly with the number of simulated time steps.

By contrast, the total number of rays that are traced with the proposed approach is independent of the number of simulated time steps, and it equals to the sum of the primary rays, secondary rays and the rays needed to generate the shadow maps. Therefore, the total number of rays needed to evaluate *p* test points with the proposed approach is:

$$R_2 = p \left(r + r^2 + r_m + r \, r_m^2 \right) + m \, r_m \tag{C2}$$
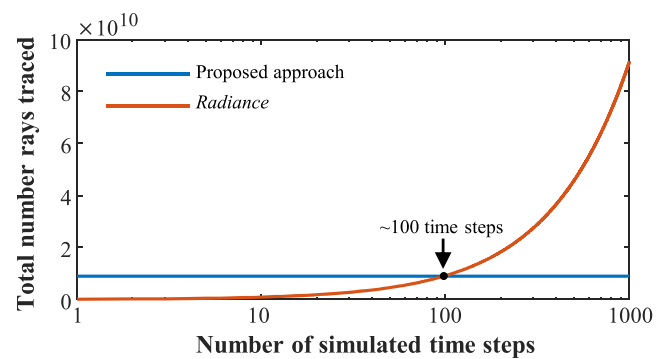
FIGURE C1 Required number of rays for a typical simulation of a 72-cell PV module. The number of required rays is approximated using Equations (C1) and (C2) where $r = 900$, $r_m = 32400$, $p = 288$ and $m = 10000$

where r is the number of rays cast in each primary and secondary samplings, r_m is the number of rays cast to create each shadow map, and m is the number of shadow maps to solve the irradiance at secondary intersection points. For shadow maps with an angular resolution of $1°$, $r_m = 360 \times 90$. Since shadow maps at secondary intersection points are cached, typically less than 10000 shadow maps are enough to calculate the irradiance on all secondary intersection points.
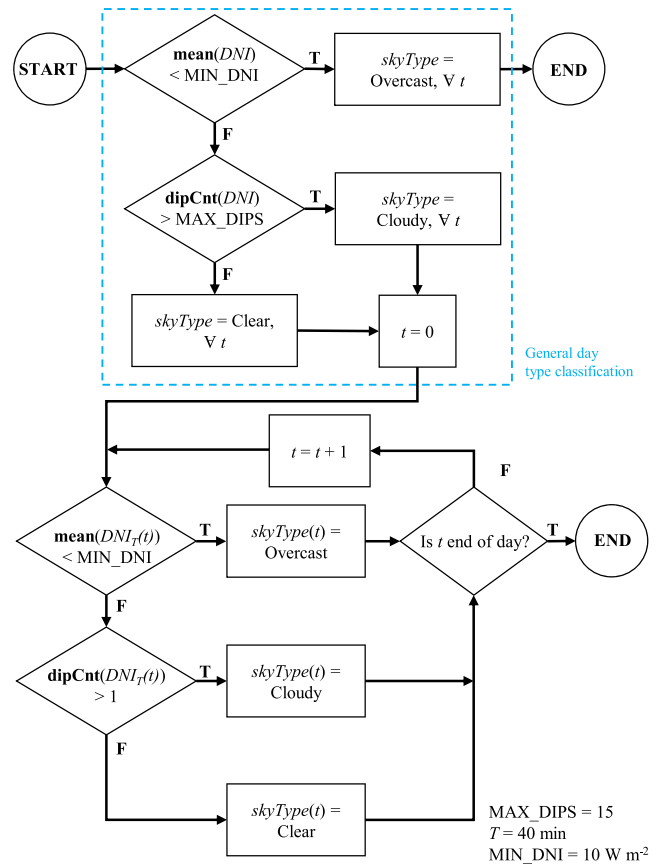
Figure C1 shows a comparison between the total number of rays required by *Radiance* (using the program *rtrace*) and the proposed approach for simulating a PV module with 72 solar cells and 4 test points per cell. The figure shows that the ray tracing calculations with the proposed approach take about the same time as 100 *rtrace* executions. In other words, the proposed approach is faster than using *rtrace* when simulating more than 100 time steps.

It should be noted that, when performing irradiance simulations in scenes with invariant optical properties, the daylight coefficient method is relatively faster compared to the proposed approach. As daylight coefficients can be calculated applying a stochastic and adaptive hemispherical sampling method, less rays need to be traced compared to the deterministic hemispherical sampling in the proposed approach. On the other hand, when performing spectrally resolved irradiance simulations, the computation time of the daylight coefficient method increases linearly with the number of spectral bands and is significantly higher than that of the proposed approach.

APPENDIX D: SPECTRAL MODELS

SBDART allows to model the effect of clouds on the sunlight spectrum. Beam and diffuse spectra for three generic sky conditions (clear, cloudy and overcast) have been generated using SBDART for the results presented in Section 4.4. These spectra were then used as an input to the proposed irradiance simulation approach.

The sky classifier algorithm in Figure D1 is proposed to distinguish the sky condition at each simulated time instant. A two-step approach is used to count dips in the daily *DNI* time series and select one of the three sky conditions at each time instant. As a first step, the dominant sky condition during the day is identified. Then the *DNI* time series is further evaluated by applying a 40 min moving window to account for variations in cloud cover throughout the day.

The values of the parameters used to generate the spectra with SMARTS and SBDART are listed in Tables 3 and 4, respectively.

FIGURE D1 Simple *DNI*-based sky classifier algorithm. The function dipCnt determines the number of dips in a time series. $DNI_T(t)$ indicates an interval of the *DNI* time series with length T and centred at instant t